The Astrophysical Journal, 720:130–143, 2010 September 1 doi:10.1088/0004-637X/720/1/130

FIRST COMPLETE DETERMINATION OF PLASMA PHYSICAL PARAMETERS ACROSS A CORONAL MASS EJECTION-DRIVEN SHOCK

A. Bemporad and S. Mancuso
Istituto Nazionale di Astrofisica (INAF), Osservatorio Astronomico di Torino, Strada Osservatorio 20, 10025 Pino Torinese, Torino, Italy; bemporad@oato.inaf.it
Received 2010 May 19; accepted 2010 June 23; published 2010 August 6

ABSTRACT

We report on the study of a fast coronal mass ejection (CME)-driven shock associated with the solar eruption of 2002 March 22. This event was observed in the intermediate corona both in white light and the extreme ultraviolet (EUV) by the LASCO and UVCS instruments on board the *Solar and Heliospheric Observatory*, as well as in metric and decametric wavelengths through space- and ground-based radio observatories. Clear signatures of shock transit are (1) strong type II emission lanes observed after the CME initiation, (2) strong O VI λλ1032, 1037 line profile broadenings (up to $\sim 2 \times 10^7$ K) associated with the shock transit across the UVCS slit field of view, and (3) a density enhancement located in LASCO images above the CME front. Since the UVCS slit was centered at 4.1 $R_\odot$, in correspondence with the flank of the expanding CME, this observation represents the highest UV detection of a shock obtained so far with the UVCS instrument. White-light and EUV data have been combined in order to estimate not only the shock compression ratio and the plasma temperature, but also the strength of the involved coronal magnetic fields, by applying the Rankine–Hugoniot equations for the general case of oblique shocks. Results show that, for a compression ratio $X = 2.06$ as derived from LASCO data, the coronal plasma is heated across the shock from an initial temperature of 2.3×10^5 K up to 1.9×10^6 K, while at the same time the magnetic field undergoes a compression from a pre-shock value of ∼0.02 G up to a post-shock field of ∼0.04 G. Magnetic and kinetic energy density increases at the shock are comparable (in agreement with the idea of equipartition of energy), and both are more than two times larger than the thermal energy density increase. This is the first time that a complete characterization of pre- and post-shock plasma physical parameters has been derived in the solar corona.

Key words: line: profiles – shock waves – Sun: coronal mass ejections (CMEs) – Sun: radio radiation

Online-only material: color figures

1. INTRODUCTION

Measuring important coronal plasma properties such as the electron density and magnetic field distributions is essential in order to solve most of the open questions in the physics of the solar corona. In this light, the combined analysis of white-light, radio, and extreme ultraviolet (EUV) spectral signatures can represent a powerful and unique tool with which to obtain important information about the main coronal plasma physical parameters at distances from the Sun that have not yet been directly accessed by spacecraft.

Particularly suitable coronal diagnostics are provided by the analysis of the radiation emitted by the local plasma during the passage of coronal shock waves (e.g., Mancuso et al. 2003). The formation of fast-mode magnetohydrodynamic (MHD) forward shocks preceding coronal mass ejections (CMEs) depends on the difference in speed between the faster CMEs and the slower solar wind in the corona. When this difference is larger than the local magnetosonic speed, fast-mode MHD shocks are produced ahead of the CMEs (e.g., Lin et al. 2006). In general, type II radio bursts are the clearest signatures of shock waves traveling through the solar corona. Type II radio emission appears in dynamic spectra as narrow bands of enhanced radio emission slowly drifting in frequency. They are attributed to shock-accelerated beams of electrons that excite electron plasma (Langmuir) oscillations which in turn non-linearly convert into escaping electromagnetic waves close to the local plasma frequency $f_{\rm pe}$ and its harmonics (Wild 1950; Nelson & Melrose 1985). The emission observed at the plasma frequency relates directly to the local electron number density n_e ($f_{\rm pe} \sim 9\sqrt{n_e\,({\rm cm}^{-3})}$ kHz), and thus to the burst driver's height under the assumption of a suitable coronal density model. Since the electron density, and consequently the plasma frequency, decreases outward from the Sun, type II radio emission typically drifts to lower frequency.

Although spectral observations of coronal type II radio bursts are very common throughout the solar cycle (e.g., Gopalswamy 2006), they fail to provide spatial information about the actual location of the shock in the corona and analyses of radio spectra only yield some details about the properties of the shocked plasma. Moreover, direct imaging of coronal shocks remains an outstanding observational challenge. Detections of metric type II radio bursts by means of ground-based radioheliographs are in fact quite rare and known to be heavily affected by propagation effects such as refraction by large-scale coronal structures (Duncan 1979), while their identification with observed features in coronagraphic white-light images is often problematic, due to the uncertainty in differentiating between hot, shock-compressed plasma, and ejected prominence material. Finally, both radio and white-light observations do not yield information about the mechanism for heating of the shocked coronal plasma. It is thus essential for this purpose to use remote-sensing observations that are sensitive to both kinetic and thermal effects produced on the plasma by the passage of the shock.

In the past decade, ultraviolet spectroscopy has been effectively used for shock detection and modeling, also providing many unique diagnostics. UV spectroscopic observations have not only the potential of detecting the spatial location and timing of coronal shocks but can also yield unique information on

the heating process of the plasma behind the shock. The first CME-driven shock detected with the Ultraviolet Coronagraph Spectrometer (UVCS; Kohl et al. 1995) on board the *Solar and Heliospheric Observatory* (*SOHO*) spacecraft was observed at 1.75 $R_\odot$ on 1998 June 11. In this event, the observed Si XII λ520 spectral line intensity roughly doubled, the O VI λ1032 line brightened by about 25%, and the H I Lyα λ1216 faded by about 10% (Raymond et al. 2000). These spectral characteristics were interpreted in terms of modest compression and ionization of the plasma and reduction of the radiative scattering components of the Lyα by Doppler dimming, due to the Doppler-shifted chromospheric radiation that can no longer be scattered by the radiatively dominated moving neutral atoms. A second UVCS CME/shock, observed at 1.6 $R_\odot$ on 2000 March 3, was analyzed by Mancuso et al. (2002). This event showed similar changes, with such broad O VI spectral line widths that the shock apparently randomized the bulk velocity of the particles, with little thermal equilibration. In the above best observed cases, the ionization time was comparable to the total time the shocked plasma was observed, the electron heating was quite modest, and the ion temperature increase was consistent with mass-proportional heating. Other events with similar properties were later discovered in the UVCS spectra and analyzed by Raouafi et al. (2004) and Ciaravella et al. (2005, 2006). Spectral analysis of the O VI lines of the 2002 July 23 event by Mancuso & Avetta (2008) further suggested that the ambient plasma β could be a key parameter in the heating of ions at coronal shocks.

In the present work, we analyze a CME/shock event observed at 4.1 $R_\odot$ with the UVCS instrument during solar maximum conditions. The shock produced clear signatures in the radio data, in the EUV spectra, and in the white-light coronal images. By means of the above-mentioned observations, we will derive a number of key plasma parameters that will allow us to retrieve, through application of the MHD Rankine–Hugoniot jump relations for oblique shocks, the full set of physical parameters characterizing the plasma involved in the shock. We first describe the observations and the shock signatures in radio, white-light, and EUV data (Section 2); in Section 3, we derive the main physical parameters of the pre-shock coronal plasma, which are employed in Section 4 to derive the post-shock physical parameters through the MHD Rankine–Hugoniot jump relations for oblique shocks; our results are summarized and discussed in Section 5.

2. OBSERVATIONS AND DATA ANALYSIS

2.1. Coronal Mass Ejection and Flare Activity

On 2002 March 22, a fast CME event was detected in white light by the Large Angle Spectrometric Coronagraph (LASCO; Brueckner et al. 1995) on board *SOHO*. The CME was associated with an M1.6 class flare originating at 10:12 UT from active region (AR) NOAA 9866, located at the West Limb, with peak emission at 11:14 UT. The CME leading edge was first observed in white-light LASCO/C2 images at 11:06 UT (Figure 1, top left panel). Subsequent images show a bright front (Figure 1, top middle and right panels), expanding westward at ∼1750 km s^{-1} (as reported in the online LASCO CME Catalog; Gopalswamy et al. 2009), followed by a more dispersed expanding plasma. In these images, the position of the prominence-related CME core is not clearly identifiable. The extrapolation to the solar surface of a linear fit to the height–time CME trajectory yields an onset time at 10:52 UT, well after the flare's onset but about 20 minutes before the soft X-ray peak emission. This event was also associated with a mild, gradual solar proton event measured by the *GOES* spacecraft, starting at 20:20 UT on March 22 and ending at 13:20 UT on March 23, with an average proton flux of 16 particle flux units (pfu).

2.2. Radio Observations

The first signature of propagation of a CME-driven shock was the associated strong, complex metric/decametric type II radio bursts. Metric type II emission was reported in the Solar Geophysical Data (SGD) by the Izmiran digital radio spectrograph (Gorgutsa et al. 2001) as a harmonic starting at 10:47.0 UT at 210 MHz and ending at 10:48.1 UT at 105 MHz. The same emission was also observed by the Astrophysical Institute Potsdam (Germany) radio spectrometer (Mann et al. 1992) as a complex type II radio burst feature (Figure 2, top panel) and it was imaged in the 164 MHz band by the Nançay Radioheliograph (NRH; The Radioheliograph Group, 1993). The radio images (Figure 3, middle panels) acquired by NRH approximately 30 minutes after the flare onset show the formation of an arch-shaped radio emission centered ∼0.4 $R_\odot$ above the limb approximately at the latitude of the CME source region. A comparison with a Fe XII λ195 difference image obtained nearly at the same time by the Extreme-ultraviolet Imaging Telescope (EIT; Delaboudinière et al. 1995) on board *SOHO* shows that this metric radio emission is located just above the region where the coronal plasma has been evacuated (Figure 3, right panel) leading to the CME. The 164 MHz emission detected by NRH is strongly suggestive of the plane-of-the-sky section of a CME-driven coronal bow-shock surface. At lower frequencies, strong and complex decametric type II emission associated with the same event was also observed slowly drifting in the outer corona by the RAD2 receiver (covering frequencies from 1.075 MHz to 13.825 MHz) of the Radio and Plasma Waves (WAVES) experiment on board the WIND spacecraft (Bougeret et al. 1995). The bright, multi-component type II emission (Figure 2, bottom left panel), indicates that the shock surface was further piston-driven outward in the solar wind, but with the radio emission originating from different portions of the shock surface.

In order to estimate the shock speed from the above observations, the relationship between the electron density and the height above the corona has to be known or at least assumed. It is well established observationally that the interplanetary type II radio emissions occur just upstream of the shock (Cairns 1986; Reiner et al. 1997; Thejappa et al. 1997; Bale et al. 1999; Knock et al. 2001). Thus, type II radio emissions refer to the pre-shocked plasma. The most widely used electron density models in type II-related studies are the radial profiles derived by Newkirk (1961) and Saito (1970), with the former model usually applied below about ∼2 $R_\odot$ and the latter between about 1.5 and 10 $R_\odot$. The two models agree quite well in the middle corona whenever the Saito (1970) profile is multiplied by a factor of 2.5. By using the observed frequency drift rate of the metric type II emission from Izmiran and assuming the Newkirk (1961) electron density model between 1.25 and 1.5 $R_\odot$, we obtain an average shock speed of about 2700 km s^{-1}, that is a factor ∼1.5 higher than the CME speed (1750 km s^{-1}) as deduced from a linear fit to the LASCO data. We point out that Izmiran also reported simultaneous (probably shock-associated) type III emission occurring around the same interval of time but in a wider frequency range, from 210 MHz to 40 MHz. Due to the extended temporal scale of the figure presenting the dynamic spectrum from Potsdam (Figure 2, top panel) and because of the brief time interval of emission of the quickly drifting type II feature

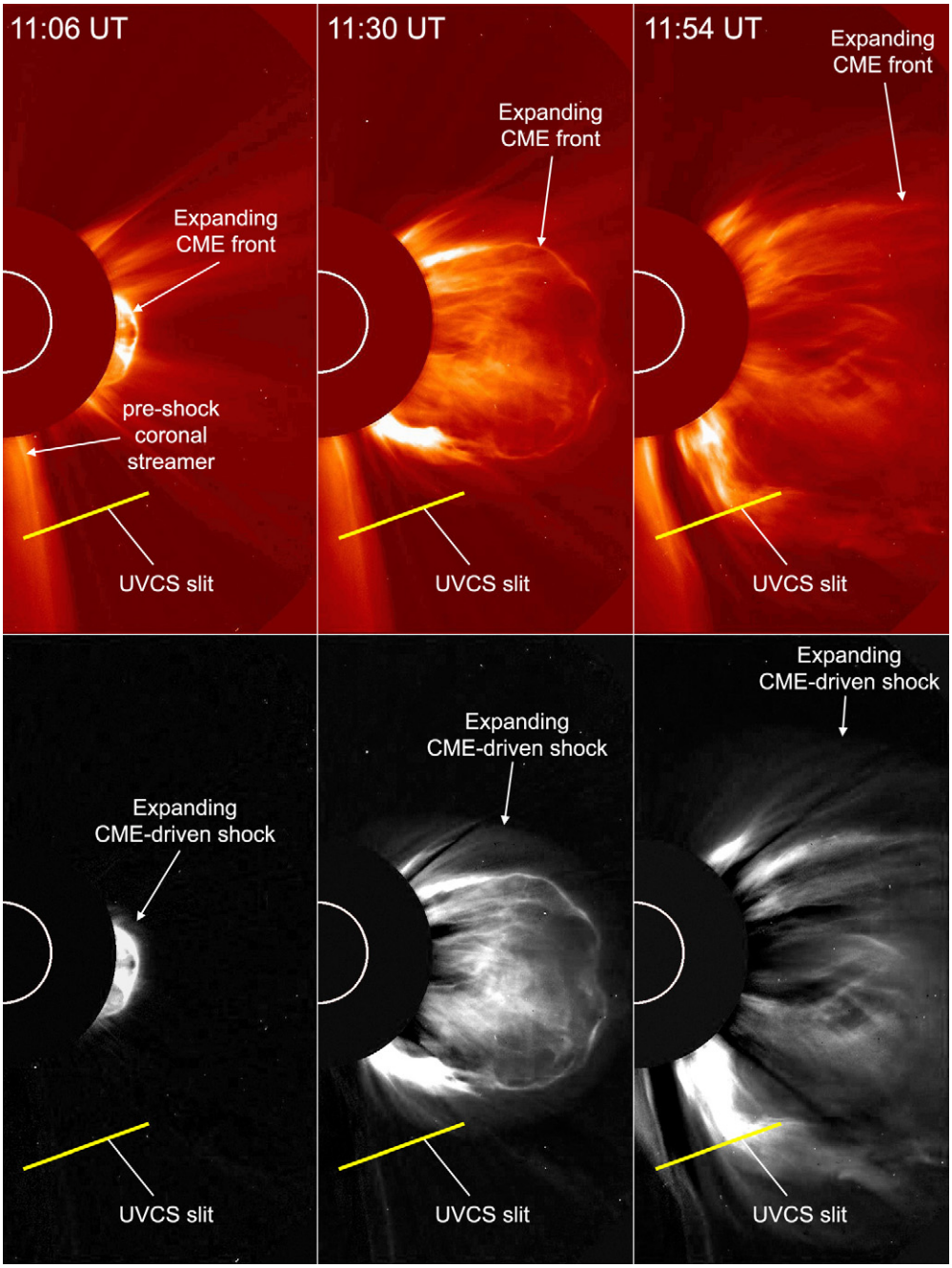

Figure 1. Sequence of LASCO/C2 standard (top) and base difference (bottom) images showing the evolution of the CME on 2002 March 22; the solid yellow line shows the position of the UVCS slit FOV, centered at 4.1 $R_{\odot}$. Comparison between standard and base difference images reveals the existence of a nearly hemispherical density enhancement located above the CME front: we identified this as the compression due to the passage of the CME-driven shock. Hence, this sequence shows the position of the shock front before (left, 11:06 UT), during (middle, 11:30 UT), and after (right, 11:54 UT) its passage through the UVCS slit.

(A color version of this figure is available in the online journal.)

reported by Izmiran, the two simultaneous emissions are difficult to disentangle by eye. The arrows superposed on the Potsdam spectrum in Figure 2 (top panel) point to the above-mentioned features, in order to help the reader identify the various emissions and their different origins. A subsequent type II radio burst was also observed drifting from 70 MHz at 11:08.4 UT to 55 MHz at 11:10.6 UT. This feature is also clear in the Potsdam spectrum. Again, using the Newkirk (1961) density model and assuming emission from the harmonic, we obtain a speed of about 800 km s^{-1}, much less than the estimated CME speed at the corresponding height (1.7–2.0 $R_{\odot}$). The observed metric dynamic spectrum thus shows a double type II radio burst, whose origin could be attributed to emission from the shock front (as evinced from the simultaneous Nançay Radioheliograph images at 164 MHz at about 10:48 UT) and (subsequently) from a flank of the shock surface interacting with a different streamer structure and thus propagating at a much lower speed (e.g., Mancuso & Abbo 2004; Mancuso & Raymond 2004; Mancuso 2007; Mancuso & Avetta 2008). Later in this work, we will show that the estimated shock speed from this latter component is actually in agreement with the one obtained through LASCO and UVCS data in the coronal region studied in this work.

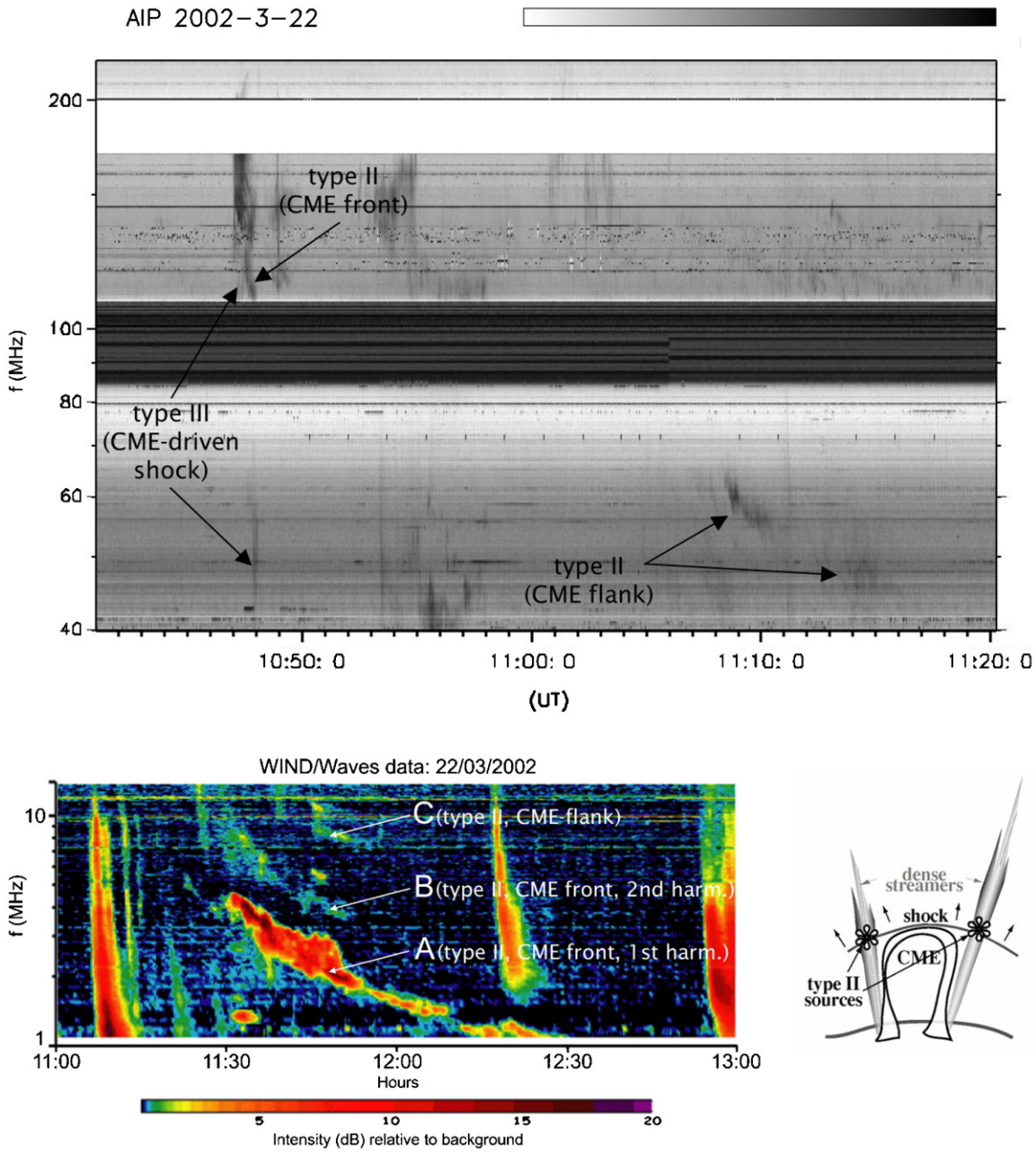

Figure 2. Top: complex type II radio burst features observed by the radio spectrometer at the Astrophysical Institute Potsdam (Germany); the spectrum shows a first component starting at 10:47.0 UT at 210 MHz and ending at 10:48.1 UT at 105 MHz (1) and a second component drifting from 70 MHz at 11:08.4–11:10.6 UT at 55 MHz ((2); see the text). Bottom: the type II radio burst associated with the CME as observed by the WAVES RAD2 experiment onboard the WIND spacecraft at 1–14 MHz between 11:00 and 14:00 UT. A strong type II burst fundamental lane is observed from about 11:30 until 12:20 UT (A), accompanied by two simultaneous fainter type II burst lanes observed at higher frequencies until about 13:20 UT (B-C). The observed A-B type II radio burst lanes can be ascribed to the first (A) and second (B) harmonic of the radio emission associated with the expansion of the CME front, while the third type II lane (C) can be associated with the collision between the CME-driven shock and the nearby coronal streamer (see also the right illustration from Reiner et al. 2003).

(A color version of this figure is available in the online journal.)

The decametric dynamic spectrum from WIND/WAVES shows multiple type II emission lanes at the fundamental and second harmonic, as well as band-splitting and embedded type III radio bursts (Figure 2, bottom left panel). The fundamental band of the most prominent type II emission lane (identified with A in Figure 2, bottom left panel) brightens at about 11:30 UT at a frequency of around 4 MHz and drifts down to ∼1.5 MHz in about half an hour. Assuming a 2.5 × Saito (1970) profile (for consistency with the profile used in the metric range), we obtain a shock speed of about 1700 km s^{-1}, comparable to the speed of the CME leading edge. Simultaneously, another pair of type II emission lanes can be clearly seen at higher frequencies (identified with B and C in Figure 2, bottom left panel), with the highest one drifting from about 12 MHz at 11:35 UT to ∼2.5 MHz around 13:20 UT. These lanes might be attributed to the fundamental (or harmonic) lane of the second type II observed in the metric band and associated with the flank of the shock surface impacting with a dense streamer at about 3.4 $R_{\odot}$ (see the illustration in Figure 2, bottom right panel). In fact, by applying the 2.5 × Saito (1970) density model to this (harmonic) lane (the fundamental, lane B, is mixed with the second harmonic of lane A), we obtain a shock speed of

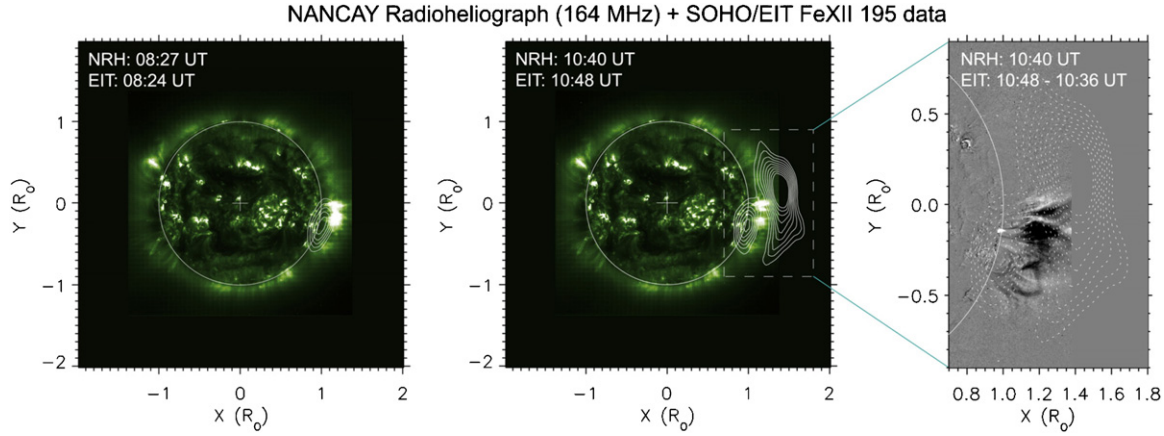

Figure 3. Comparison between the EUV Fe XII λ195 and the radio 164 MHz emission observed, respectively, by the *SOHO*/EIT telescope and the Nançay Radioheliograph before (left) and during (middle) the CME. The left panel shows that, before the flare (onset at 10:12 UT), 164 MHz radio emission is associated solely with the source AR, while after the flare a bright arch-shaped front appears centered at 0.4 $R_\odot$ above the limb approximately at the same latitude than the source AR (middle panel). A superposition (right panel) with the running difference EIT image (showing as bright/dark regions the density enhancements/depletions) demonstrates that this additional radio emission is located exactly above the coronal region from where the plasma has been evacuated, in front of the erupting CME.

(A color version of this figure is available in the online journal.)

about 800 km s^{-1}, that is, the same speed of the metric feature observed in the metric radio dynamic spectrum. Actually, we will see that both in the LASCO in the UVCS images the deflection of the streamer in the southern region next to the end of the UVCS slit reached by the shock surface appears around the time (and inferred height) of the appearance of the third lane feature in the decametric spectrum, thus corroborating the latter interpretation. As pointed out by Ontiveros & Vourlidas (2009), deflections of coronal streamers provide the best imaging signature in white light for CME-driven shocks (Gosling et al. 1974; Sheeley et al. 2000; Vourlidas et al. 2003).

For completeness we mention that an alternative interpretation, with the three parallel lanes observed by WIND/WAVES representing the first, second, and fourth harmonic, cannot be completely discarded on the basis of the available observations (N. Gopalswamy 2009, private communication). We point out, however, that the emission from lane C seems too intense (apparently as much as the harmonic lane) to be attributed to a fourth harmonic component.

2.3. White-light Observations

The second clear signature of a CME-driven shock is provided by the LASCO white-light images. As recently demonstrated by Ontiveros & Vourlidas (2009), base difference images (obtained by subtracting from each image the last one before the CME appearance) can be used to identify shock signatures in white-light images and distinguish between shock-compressed plasma and CME material. In particular, the base difference image at 11:30 UT (Figure 1, bottom middle panel) shows an enhanced arch-shaped white-light intensity region located above the expanding CME front. This feature corresponds to an increase in the column density integrated along the line of sight (LOS). In this work, in agreement with the previous interpretation by Ontiveros & Vourlidas (2009) for similar events, we interpreted this enhanced density as the downstream plasma compressed by the transit of the CME-driven shock.

As we will discuss in the next paragraph, LASCO/C2 images can be used to infer the compression ratio X between the downstream (ρ_d) and upstream (ρ_u) plasma densities $X = \rho_d/\rho_u$, which is of paramount importance in order to determine all the other physical parameters of the shocked plasma. LASCO images also show that the southward coronal streamer is deflected by the arrival of the CME-driven shock (frames at 11:54 UT). Such a deflection is also clearly observed in the EUV spectra acquired by UVCS. As already mentioned, streamer deflections provide the best shock signature in white light. An approximate estimate of the shock speed projected on the plane of the sky $v_{\rm sh(POS)}$ can be derived from two consecutive LASCO/C2 base difference images (Figure 1, bottom panels). It turns out that, at the latitude of ∼57°S where the shock front crossed the UVCS slit at 11:30 UT, the shock propagated at $\sim v_{\rm sh(POS)} \simeq 1030$ km s^{-1} (with respect to a shock velocity on the equatorial plane of ∼1700 km s^{-1}). Nevertheless, these values are only approximated, because of the very low LASCO frame rate (about 24 minutes). A more accurate estimate of the shock velocity at the UVCS altitude will be derived from the observed evolution of EUV intensities.

2.4. EUV Observations

The third definite signature of shock transit is provided by the observed EUV coronal spectra. During the CME expansion, UVCS was observing above the southwest limb with the entrance slit centered at a latitude of 70° SW at a heliocentric distance of 4.1 $R_\odot$(Figure 1). The entire set of observations comprised 171 exposures of 200 s each, starting from 08:20 to 18:29 UT, encompassing the whole CME/shock event. The most prominent spectral lines detected during this time interval were the O VI λλ1031.9, 1037.6 doublet and the H I Lyα λ1215.67 lines, while other spectral lines produced only a very weak signal because of the high heliocentric distance where these data have been acquired.

From LASCO/C2 base difference images, we expect to observe a signature of the shock transit in the UV spectra at 4.1 $R_\odot$ around 11:30 UT (Figure 1, bottom middle panel). This is confirmed by the evolution of the Lyα and O VI line intensities and line profiles observed during the passage of the shock front through the UVCS slit (Figure 4). At the shock transit, the Lyα line was dimmed (Figure 4, left panel), while the O VI line intensities were suddenly enhanced (Figure 4, right panel). This different behavior was expected and is related to the different formation processes of these two lines. In typical coronal plasma conditions, the H I Lyα line is solely due to the

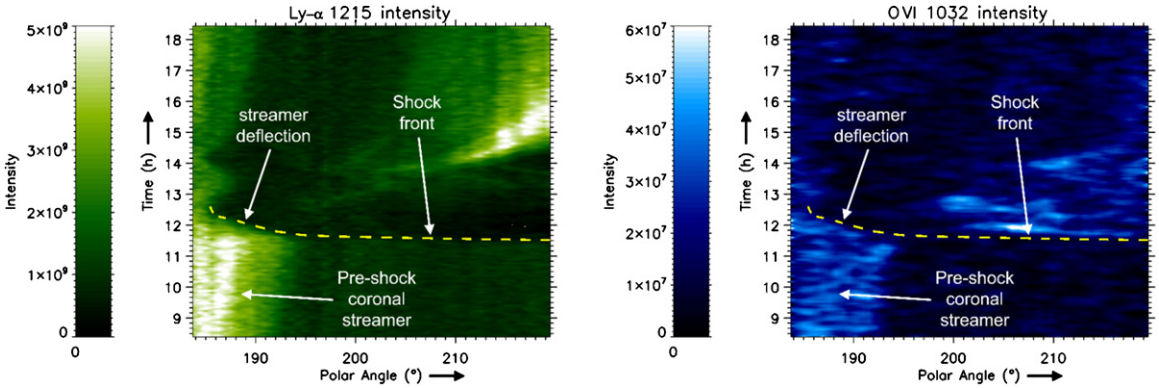

Figure 4. Space–time dependence of the Lyα λ1216 (left) and O VI λ1032 (right) line intensities observed during the passage of the shock front (dashed yellow line) through the UVCS slit. The position along the slit of a pre-CME streamer (also visible in the LASCO standard images) is also shown. The shock enters the slit from the right edge (larger polar angle), then propagates through the slit and finally collides with the southwest coronal streamer deflecting it.

(A color version of this figure is available in the online journal.)

resonant scattering of photons emitted from the underlying layers of the solar atmosphere (radiative excitation), while the O VI lines are also excited by collisions of the O^{5+} ions with thermal electrons (collisional excitation). The radiative component of each line is roughly proportional to the local electron number density n_e and is also dependent on the outflow radial velocity component v_r. As v_r increases, the chromospheric Lyα line profile (responsible for the radiative excitation) becomes Doppler-shifted with respect to the atomic absorption profile, thus reducing the efficiency of the radiative excitation and hence of the observed intensity (Doppler dimming effect). On the contrary, the collisional component of each line, roughly proportional to n_e^2, is independent of the outflow velocity of the emitting plasma. Hence, since the post-shock plasma is expected to be compressed, heated, and accelerated with respect to the pre-shock plasma, the transit of the shock corresponds to a decrease of the H I Lyα line brightness (Figure 4, left panel) and of the O VI line radiative component. Such a decrease, due to the Doppler dimming effect, leads to a much larger intensity reduction than the intensity increase implied by the plasma compression alone. On the other hand, the O VI line collisional component is not affected by Doppler dimming and increases as $\sim n_e^2$, leading to the observed O VI λ1032 post-shock intensity increase (Figure 4, right panel). As time goes on, the Lyα and O VI intensity evolutions also show the deflection of the southward streamer visible in LASCO white-light images.

The spectral line intensity evolutions described above are not the only effect on EUV spectra expected after the shock transit. We already mentioned that previous detections in UVCS data of CME-driven shocks (e.g., Raymond et al. 2000; Mancuso et al. 2002) demonstrated that strong broadenings of the O VI line profiles are also observed. These broadenings are actually theoretically expected because of the plasma heating occurring across the shock (e.g., Pagano et al. 2008). All previous UVCS observations reported shocks that were typically detected below the heliocentric distance of 2 $R_\odot$, with strong broadenings observed in only a few exposures during the shock transit across the slit. On the contrary, the shock reported in this work has been observed at 4.1 $R_\odot$, where the number of observed counts is much smaller. For this reason, in a preliminary inspection of the line profiles, we time-averaged the data over a few exposures and thus, because of the low statistics, we were not able to identify any clear line broadening. In the following analysis, however, we increased the statistics by averaging the spectra both in space and time, that is, over 60 arcsec (corresponding to 10 spatial bins) and 30 minutes (corresponding to nine exposures), respectively. The resulting average normalized profiles are shown in Figure 5, together with the pre-shock line profiles. The post-shock profiles have been obtained after subtraction of the pre-shock profiles in order to remove the emission, through the optically thin corona, of the unshocked plasma aligned with the UVCS LOS and located behind and/or below the shocked plasma. Profiles in Figure 5 show that the post-shock O VI line profiles (top left panel, solid line) are not only broadened, but also Doppler-shifted with respect to the pre-shock coronal profiles (top left panel, dotted line); in the following hours, both effects progressively fade, and the pre-shock line width and centroid position are recovered (Figure 5, bottom right panel).

By applying a standard Gaussian fit to the pre- and post-shock line profiles, we derived the evolution of the O^{5+} ion kinetic temperature T_k (Figure 6, top left panel) and LOS velocity $v_{\rm sh(LOS)}$ (Figure 6, top middle panel). In particular, the plot in Figure 6 (top left panel) shows that, about 30 minutes after the shock, T_k increased by a factor $\sim$2 with respect to the pre-shock value and, in the following 3 hr, the pre-shock temperature is recovered. Nevertheless, this is only an upper limit to the real heating that occurs across the shock. In fact, since the shock front is also expanding with velocity components aligned with the LOS, photons emitted from different parts of the post-shock plasma will be redshifted or blueshifted, thus leading, by integration across the optically thin coronal plasma, to a broader profile (Figure 6, bottom illustration). For instance, Ciaravella et al. (2006) concluded that, for some fast events, broadenings observed in the O VI lines can be entirely ascribed to the LOS component of the bulk expansion and a similar evolution of the O VI line width has also been found by Bemporad et al. (2007) for a slow CME (i.e., not associated with a CME-driven shock). Hence, both increasing temperature and expansion of the emitting volume contribute to broadening the line profiles, and the effect of bulk motions can be removed only by assuming a three-dimensional expansion model for the shock surface (e.g., Mancuso & Avetta 2008). The plots in Figure 6 (top middle panel) also show that the observed O VI Doppler redshift corresponds to $v_{\rm sh(LOS)} \simeq 120$ km s^{-1}. This shift is likely due to an inclination angle $\theta_{\rm sh}$ of the shock front with respect to the plane of the sky, as shown in Figure 6 (bottom image). This velocity corresponds to a shock inclination angle $\theta_{\rm sh} = \arctan(v_{\rm sh(LOS)}/v_{\rm sh(POS)}) \simeq 7^\circ$. Hence, to a first approximation, the shock is expanding parallel to the plane of the sky.

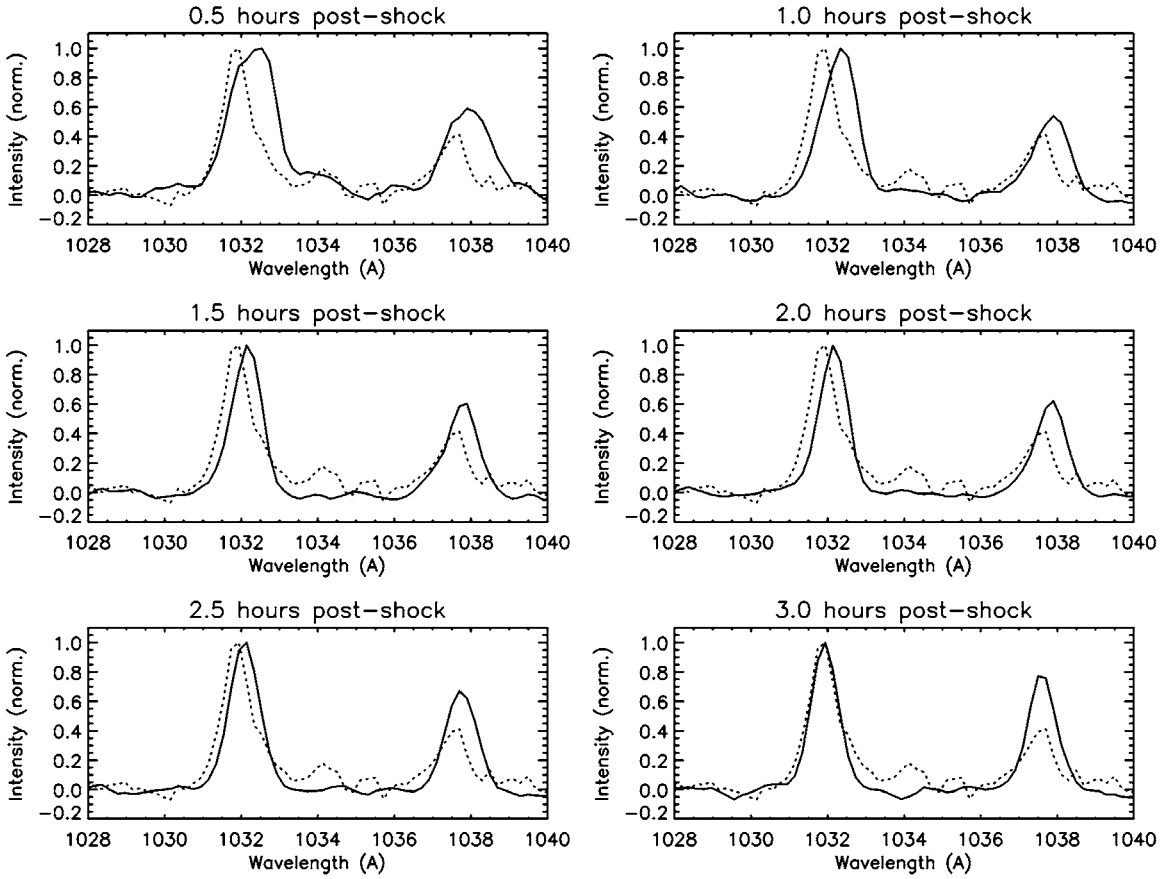

Figure 5. Evolution of the O VI λλ1031.9, 1037.6 normalized line profiles of shocked plasma (solid line) with respect to the pre-shock coronal profiles (dotted line). Profiles averaged over the first 30 minutes after the shock transit are broadened and Doppler-redshifted with respect to the coronal profiles; in the following ∼3 hr the line profile broadening and Doppler shift progressively fade with time. Even if the pre-shock line profile width and centroid position are eventually recovered after ∼3 hr (see also Figure 5), the post-shock ratio between the 1032/1037 line intensities is much smaller than what observed in the pre-shock plasma (bottom right panel): this is indicative of large outflow velocities present even hours after the shock transit (see the text).

Interestingly, the O VI line profiles (Figure 5) show that, even though the pre-shock kinetic temperature and LOS velocity are recovered 3 hr after the shock transit, a clear signature of shocked plasma acceleration is still present. In fact, the O VI 1032/1037 line intensity ratio $r_{\rm O\,VI}$ is directly related to the radial component of the plasma velocity. More specifically, the collisional components of the O VI lines have an intensity ratio $r_{\rm O\,VI} = 2$, while the ratio of the radiative components is $r_{\rm O\,VI} = 4$ for emitting plasma at rest (Noci et al. 1987). As the O^{5+} ions move outward in the corona, the radiative component is Doppler-dimmed, so that the line ratio decreases, eventually becoming collisional when the outflow speed is such that the absorbing and emitting profiles no longer overlap. In particular, for a radial velocity of order $\simeq$1000 km s^{-1}, the O^{5+} absorption profile is shifted by ∼3.4 Å with respect to the chromospheric emission profile and we expect the O VI radial component to be completely Doppler-dimmed. Moreover, for large velocities (typically $v \gtrsim 100$ km s^{-1}), it is necessary to also take into account the pumping of the O VI λ1037.6 line by the C II λλ1036.3,1037.0 lines ($v \simeq 180 - 380$ km s^{-1}), by the O VI λ1031.9 line ($v \simeq 1650$ km s^{-1}) and also the pumping of the O VI λ1031.9 line by the H Lyβ λ1025.7 ($v \simeq 1800$ km s^{-1}), which lead to $r_{\rm O\,VI}$ values even smaller than 2 (see Raymond & Ciaravella 2004 for a comprehensive discussion of the Doppler dimming/pumping effect on O VI lines during CMEs). This is confirmed by the observed ratio of post-shock O VI line intensities (Figure 6, top right panel): for the pre-shock plasma, this ratio is $r_{\rm O\,VI} \simeq 2.8$ (corresponding to a pre-shock outflow speed of $\simeq$100 km s^{-1}), while in the post-shock plasma $r_{\rm O\,VI}$ decreases down to $\sim 1.3 < 2$ (corresponding to a post-shock outflow speed $v \gtrsim 400$ km s^{-1}); higher values of $r_{\rm O\,VI}$ are eventually recovered 6 hr after the shock transit. Hence, the UVCS data also provide a direct signature of post-shock plasma acceleration.

3. DETERMINATION OF PRE-SHOCK PLASMA PARAMETERS

In this section, we will describe how white-light and EUV data relative to the CME-driven shock described above have been combined in order to determine the full set of pre-shock plasma physical parameters, except for the pre-shock coronal magnetic field. In the next section, we will show how, given the pre-shock plasma parameters and the shock compression ratio X, it is possible to use the Rankine–Hugoniot equations in the general case of an oblique shock in order to estimate the full set of post-shock plasma physical parameters and also the pre-shock magnetic field.

3.1. Plasma Parameters from EUV Data

In this work, the O VI and H I Lyα intensities observed before the arrival of the shock front have been used to estimate the pre-shock electron temperature T_e and electron number density n_e (cm^{-3}), while we estimated the component of the shock velocity $v_{\rm sh(UVCS)}$ parallel to the UVCS slit from the observed intensity evolution. To this end, it is necessary to take into account the

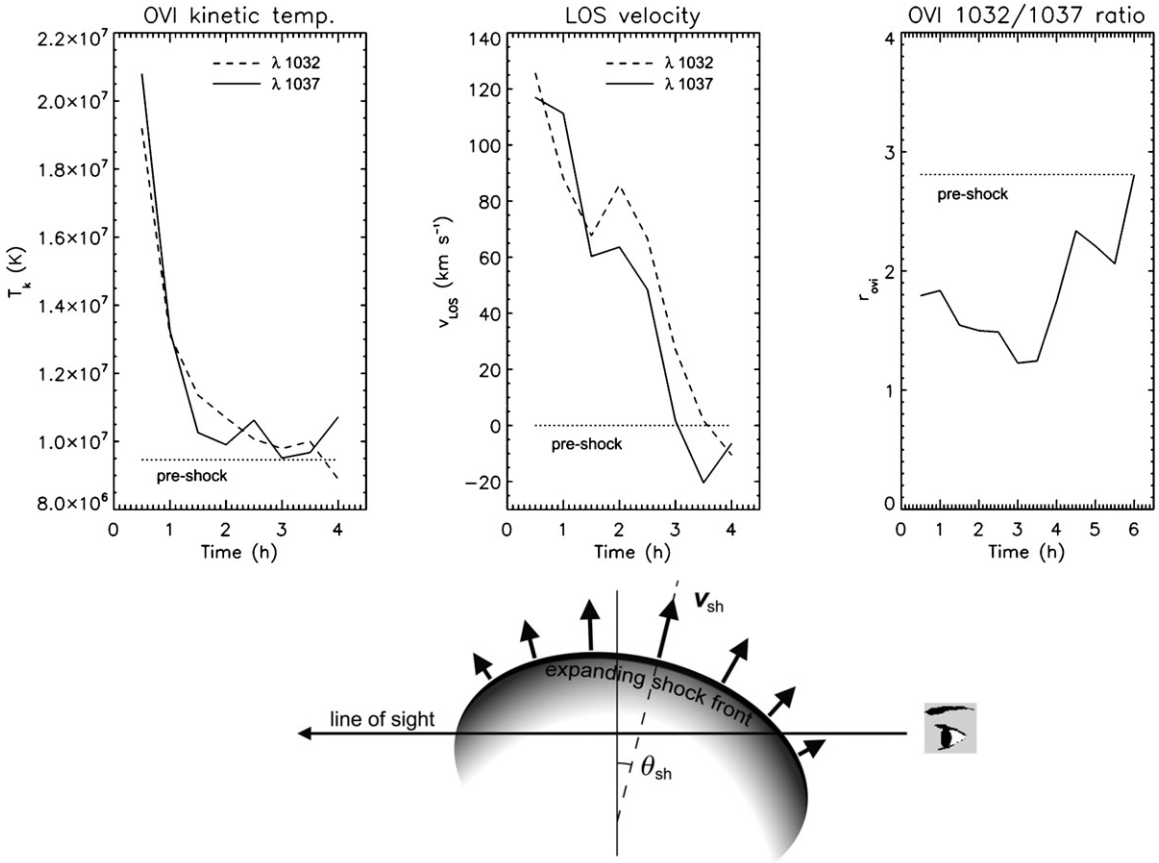

Figure 6. Top: evolution of the O^{5+} ions kinetic temperature T_k (left) and LOS velocity v_{los} (middle) as observed in the first 4 hr after the shock transit at 4.3 $R_\odot$. Left and middle plots show that ∼3 hr after the shock transit both T_k and v_{los} values observed in the pre-shocked plasma (dotted lines) are mainly recovered. Nevertheless, at this time strong outflows due to the post-shocked plasma acceleration are still present, as demonstrated by the evolution of the ratio $r_{O\,VI}$ between the O VI λλ1031.9, 1037.6 lines (right panel; see the text). Bottom: an illustration showing how an expanding shock propagating with velocity v_{sh} and an inclination angle θ_{sh} may be responsible for both the observed T_k and v_{los} evolutions.

effect of integration along the LOS at 4.1 $R_\odot$. The radiative (I_{rad}) and collisional (I_{col}) components of a spectral line can be written, to a first approximation, as

$$I_{rad} \propto \frac{\langle I_{disk}\, D(v_{out})\, R_{X+m}(T_e)\, A_X\rangle \int_{-\infty}^{+\infty} n_e\, dz}{\sqrt{\Delta\lambda_{cor}^2+\Delta\lambda_{ex}^2}}\, h(r)$$
$$I_{col} \propto \langle Q(T_e)\, R_{X+m}(T_e)\, A_X\rangle \int_{-\infty}^{+\infty} n_e^2\, dz, \quad (1)$$

where I_{disk} is the intensity of the exciting radiation emitted from the disk, $D(v_{out})$ is the Doppler dimming/pumping factor (dependent on the outflow velocity v_{out}), A_X is the absolute abundance of the element X, $R_{X+m}(T_e)$ is the ionization equilibrium for the emitting ion X^{+m}, $h(r) = 2[1-(1-1/r^2)^{1/2}]$ is the dilution factor (dependent on the heliocentric distance r expressed in $R_\odot$), $\Delta\lambda_{cor}$ and $\Delta\lambda_{ex}$ are the $1/e$ half widths of the coronal (absorption) and disk (emission) line profiles, $Q(T_e)$ is the collisional excitation rate, $z = \sqrt{r^2-\zeta^2}$ is the coordinate along the LOS at the projected altitude ζ, and the symbol $\langle F\rangle$ indicates the average of quantity F integrated along the LOS. The above equations show that, in a first-order approximation, the EUV intensity observed at each altitude depends on the unknown electron temperature T_e, electron number density n_e, and outflow velocity v_{out} profiles along the LOS, while the dependence along the LOS on the unknown elemental abundance can be neglected. In this work, we used the H I Lyα λ1215.6 and O VI λ1031.9 average intensities observed before the arrival of the shock in the UVCS slit to estimate the electron density and temperature in the pre-shock plasma. To this end, we followed this technique: first, we assumed model profiles for $T_e(r)$, $n_e(r)$, and $v_{out}(r)$ for altitudes $r \geqslant 4.1\ R_\odot$, then we multiplied the $T_e(r)$ and $n_e(r)$ profiles by two independent constant multipliers (K_T, K_n), respectively, and we computed the expected Lyα and O VI radiative and collisional intensities integrated along the LOS for a range of (K_T, K_n) pair values. By comparing the observed line intensities with those computed for each pair of (K_T, K_n) we determined the multiplier values best reproducing the observations, hence the LOS temperature and density profiles given by $K_T\, T_e(r)$ and $K_n\, n_e(r)$. Therefore, in the above technique, we did not assume the absolute values of the $T_e(r)$, $n_e(r)$, and $v_{out}(r)$ profiles, but we simply used the shapes of these profiles and we determined the absolute $K_T\, T_e(r)$, $K_n\, n_e(r)$ profiles with the same shape that was needed in order to reproduce the observed line intensities.

In particular, in the computation, we used the following constant quantities: oxygen abundance (relative to H) A_O = 8.67 dex (from Bemporad et al. 2003), $\Delta\lambda_{ex(Ly\alpha)} = 0.480$ Å and $\Delta\lambda_{ex(O\,VI)} = 0.121$ Å (respectively, from Gouttebroze et al. 1978 and Doschek & Feldman 2004), $\Delta\lambda_{cor(Ly\alpha)} = 0.565$ Å and $\Delta\lambda_{cor(O\,VI)} = 0.628$ Å as estimated from a standard Gaussian fitting to the observed coronal line profiles, $I_{disk(Ly\alpha)} = 5.2 \times 10^{15}$ phot cm^{-2} s^{-1} sr^{-1} and $I_{disk(O\,VI)} = 1.8 \times 10^{13}$ phot cm^{-2} s^{-1} sr^{-1} (respectively, from SOLSTICE satellite measurements for the same day and from Ko et al. 2008), and ionization equilibria $R_{X+m}(T_e)$ from Mazzotta et al. (1998). Pre-shock plasma parameters have been estimated

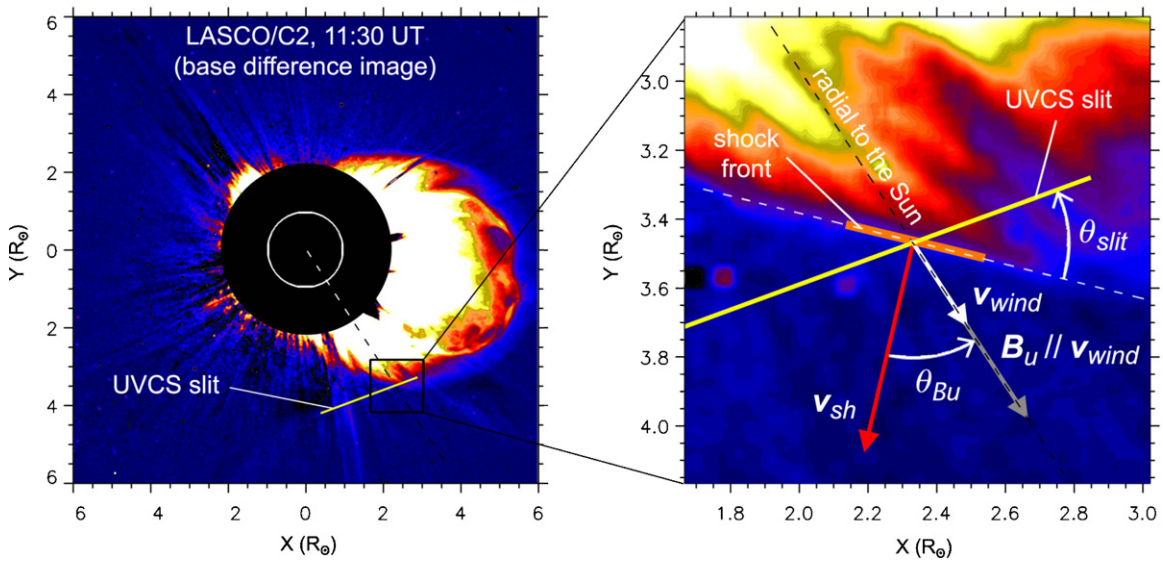

Figure 7. Left: LASCO/C2 frame at 11:30 UT shown with enhanced contrast in order to better outline the location of the shock in the coronagraph FOV with respect to the UVCS slit position. Right: a zoom over the region surrounded in the left panel by a dark box. This panel shows how from white-light 11:30 UT image it has been possible to measure the angle $\theta_{\rm slit}$ between the shock front and the UVCS slit and the angle $\theta_{\rm Bu}$ between the normal to the shock front and the magnetic field, assumed to be radial at 4.3 $R_\odot$.

(A color version of this figure is available in the online journal.)

starting from the Lyα and O VI averaged over an angular interval of $\sim$6° (10 spatial bins) at the westward edge of the UVCS slit (located at an approximate altitude of 4.3 $R_\odot$) where the shock front is observed in the LASCO/C2 11:30 UT image and over all the exposures available before the shock arrival. In particular, the pre-shock coronal intensities to be reproduced are $I_{\rm tot(Ly\alpha)} = 3.5 \times 10^9$ phot cm^{-2} s^{-1} sr^{-1} and $I_{\rm tot(O\,VI)} = 2.9 \times 10^7$ phot cm^{-2} s^{-1} sr^{-1}.

Since the westward edge of the UVCS slit is located in a high-latitude region of negligible white-light emission, we assumed coronal hole $n_e(r)$, $T_e(r)$, and $v_{\rm out}(r)$ profiles from Cranmer et al. (1999); the minimum of $v_{\rm out}(r)$ profile along the LOS has been fixed to the value of 100 km s^{-1} derived on the plane of the sky from the observed pre-shock intensity ratio $r_{\rm O\,VI}$. Given all the above quantities, it turns out that the (K_T, K_n) multipliers needed to reproduce the observed intensities are $(K_T, K_n) = (0.41, 0.56)$, which result in a density $n_e = 1.1 \times 10^4$ cm^{-3} and a temperature $T_e = 2.3 \times 10^5$ K on the plane of the sky at a heliocentric distance of 4.3 $R_\odot$.

From the observed Lyα intensity evolution during the shock transit, it is also possible to determine the component of the shock velocity $v_{\rm sh(UVCS)}$ parallel to the UVCS slit at the transit time across it. Since the shock (Figure 4) crossed 20 spatial bins, or $\simeq$6.09 $\times 10^5$ km, in two exposures, corresponding to $\simeq$418 s (by also taking into account the $\sim$9 s gap between one exposure and the next one), it turns out that $v_{\rm sh(UVCS)} \simeq 1460$ km s^{-1}. This velocity is larger than the actual shock propagation velocity $v_{\rm sh}$, which will be determined in the next section by taking into account the inclination angle between the shock front and the UVCS slit. All these plasma parameters will be used in the following sections to derive the post-shock parameters.

3.2. Plasma Parameters From White-light Data

As mentioned above, LASCO/C2 base difference images allowed us to identify the CME-driven shock as an arch-shaped density enhancement located above the expanding CME front. In this work, we used the white-light images to infer kinematical properties of the shock front. In particular, we derived the inclination angle $\theta_{\rm Bu}$ of the magnetic field vector with respect to the shock front and the actual shock propagation velocity $v_{\rm sh}$ (Figure 7). Moreover, from white-light data, we also estimated the shock compression ratio $X = \rho_d/\rho_u$, i.e., the ratio between the downstream (i.e., post-shock) and the upstream (i.e., pre-shock) densities (ρ_d and ρ_u, respectively).

Kinematical parameters of the shock front listed above can be easily determined from the LASCO/C2 base difference image at 11:30 UT (a higher contrast version is shown again in Figure 7, left panel). First, the actual shock velocity can be estimated simply as $v_{\rm sh} = v_{\rm sh(UVCS)} \times \sin\theta_{\rm slit}$, where $\theta_{\rm slit}$ is the angle between the shock front and the UVCS slit field of view (FOV; see Figure 7, right panel). With $\theta_{\rm slit} = 33\overset{\circ}{.}2$, we thus obtain $v_{\rm sh} = 800$ km s^{-1}, a smaller value than the 1030 km s^{-1} estimated in the previous section from LASCO/C2 images, which is, however, only representative of the average velocity between 11:06 and 11:30 UT. This suggests a shock deceleration during its propagation through the corona. The $v_{\rm sh}$ value derived here is in outstanding agreement with the shock speed previously estimated from radio data; this value will be used in the next section to estimate the upstream velocity v_u in a reference system at rest with the shock front. By assuming that at 4.3 $R_\odot$ (the average heliocentric distance of the UVCS slit westward edge) both the outflow velocity and the magnetic field are radial, LASCO/C2 image at 11:30 UT can be also used to derive the angle $\theta_{\rm Bu}$ between the normal to the shock front and the magnetic field vector (see Figure 7, right panel), yielding $\theta_{\rm Bu} = 46\overset{\circ}{.}1$.

In order to estimate the shock compression ratio X, it is necessary to again take into account the effects of integration along the LOS. The unpolarized white-light brightness $b(\zeta)$ observed at each pixel in LASCO images at the projected altitude ζ is produced by an integration along the LOS of the disk-emitted photons that have been Thomson-scattered by the coronal free electrons. By assuming spherical symmetry, $b(\zeta)$ can be written as

$$b(\zeta) = 2\pi\sigma_T\, b_\odot \int_0^{+\infty} n_e\, K(u, \zeta, r)\, dz, \qquad (2)$$

where σ_T is the total Thomson scattering cross section, $b_\odot$ is the mean solar surface brightness, and $K(u, \zeta, r)$ is a geometrical function dependent on the limb darkening coefficient u in the visible wavelength of interest, the projected altitude ζ of observation, and the heliocentric distance r. The integration is performed along the LOS coordinate, z. We assume that a shock with thickness L transits on the plane of the sky inducing on average an unknown density compression by a factor X and that $b(\zeta)_{\rm pre}$ and $b(\zeta)_{\rm post}$ $(>b(\zeta)_{\rm pre})$ are the white-light brightnesses observed at the altitude ζ before and after the shock transit. If $F = \int_{-L/2}^{L/2} n_e\, K(u, \zeta, r)\, dz$ is the unknown fraction of pre-shock white light emitted only from the coronal region (of thickness L along the LOS) later on crossed by the shock, the compression ratio X can be estimated as

$$X = \frac{\left[b(\zeta)_{\rm post} - b(\zeta)_{\rm pre}\right] + F\, b(\zeta)_{\rm pre}}{F\, b(\zeta)_{\rm pre}} = \frac{b(\zeta)_{\rm post} - b(\zeta)_{\rm pre}\,(1 - F)}{F\, b(\zeta)_{\rm pre}}. \quad (3)$$

In order to estimate F, the only unknown quantity in the above equation, it is necessary to assume a value for the shock thickness L along the LOS. In our previous work (Mancuso & Bemporad 2009), we estimated an upper limit to X by assuming a lower limit for $L = d_{\rm obs}$, where $d_{\rm obs}$ is the projected shock thickness as observed in LASCO image. In particular, as we concluded from the LASCO/C2 image at 11:30 UT, the white-light intensity increases across the shock front over ~6 pixels, which corresponds to a projected observed thickness $d_{\rm obs} \simeq 5 \times 10^4$ km. With this lower limit for L, it turns out that $X \leqslant 2.4 \pm 0.2$. Nevertheless, $d_{\rm obs}$ is only a lower limit for L because the shock thickness along the LOS will be larger; hence, a more accurate determination of L is needed. Actually, $d_{\rm obs}$ is larger than the real projected shock thickness $d_{\rm proj}$ because the LASCO instrument takes approximately $t_{\rm exp} = 25$ s to acquire one exposure and, during this time, the shock moved by $\Delta h = v_{\rm sh} t_{\rm exp} = 2.0 \times 10^4$ km. Hence, the real projected thickness is $d_{\rm proj} = d_{\rm obs} - \Delta h = 3.0 \times 10^4$ km $= 0.043\, R_\odot$. Now, if we assume that the shock surface can be approximated by a sphere with diameter $D \simeq 5\, R_\odot$ and thickness $d_{\rm proj}$, the LOS integration length across the shock is $L = \sqrt{d_{\rm proj}^2 + 2 d_{\rm proj} D} = 3.2 \times 10^5$ km $= 0.46\, R_\odot$. With this value of L, and by assuming along the LOS the density profile $K_n\, n_e(r)$ obtained from the UVCS data analysis, it turns out that $X = 2.06$. This value for the compression value will be important in order to characterize the shock and to determine, in the next section, the downstream plasma parameters.

4. DETERMINATION OF POST-SHOCK PLASMA PARAMETERS

The appropriate jump conditions across an MHD shock are referred to as the Rankine–Hugoniot equations. These equations are usually simplified, depending on the angle $\theta_{\rm sh}$ between the upstream magnetic field lines and the normal to the shock surface, in the two limiting cases of parallel ($\theta_{\rm sh} = 90°$) and perpendicular ($\theta_{\rm sh} = 0°$) shocks. However, under the reasonable assumption that the magnetic field at the altitude of 4.1 $R_\odot$ is already nearly radial, the LASCO/C2 images acquired on 2002 March 22 definitely show that the CME-driven shock front is strongly inclined with respect to the radial direction (Figure 7). Hence, in order to study this event and retrieve information about the parameters of coronal plasma involved in the shock, we need to apply the MHD Rankine–Hugoniot equations for the general case of an oblique shock. In a reference frame comoving with the shock surface S, with x- and y-coordinated axes, respectively, perpendicular and parallel to S (Figure 8; hereafter "RH frame"), these equations can be written (in SI units) as follows (Thompson 1962, pp. 86–95):

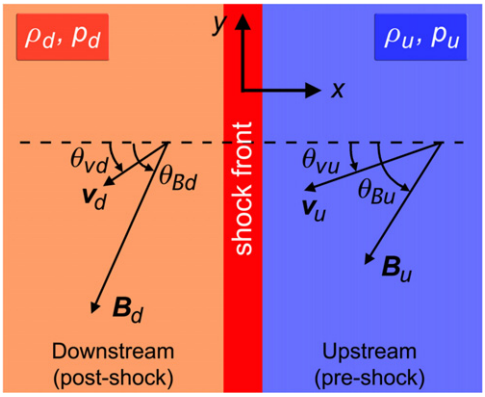

Figure 8. Rankine–Hugoniot equations are usually written in a reference system at rest with respect to the shock surface, as shown here. In this reference system, for the general case of an oblique shock, a pre-shock (upstream) plasma crosses the shock front with density ρ_u, pressure p_u, magnetic field and upstream velocity vectors $\mathbf{B}_u$ and $\mathbf{v}_u$, inclined, respectively, with angles $\theta_{\rm Bu}$ and $\theta_{\rm vu}$ with respect to the normal to the shock surface (right). The post-shock plasma (left) leaves the shock front with density ρ_d, pressure p_d, magnetic field and upstream velocity vectors $\mathbf{B}_d$ and $\mathbf{v}_d$, inclined, respectively, with angle $\theta_{\rm Bd}$ and $\theta_{\rm vd}$ with respect to the normal to the shock surface (see the text for equations).
(A color version of this figure is available in the online journal.)

$$[\rho\, v_x] = 0 \quad (4)$$

$$\left[\rho\, v_x^2 + p + \frac{B_y^2}{2\mu}\right] = 0 \quad (5)$$

$$\left[\rho\, v_x v_y - \frac{B_x B_y}{\mu}\right] = 0 \quad (6)$$

$$\left[\frac{1}{2}v^2 + \frac{\gamma}{\gamma - 1}\frac{p}{\rho} + \frac{B_y\left(v_x B_y - v_y B_x\right)}{\mu \rho v_x}\right] = 0 \quad (7)$$

$$[B_x] = 0 \quad (8)$$

$$\left[v_x B_y - v_y B_x\right] = 0, \quad (9)$$

where, as usual, $[F] \equiv F_u - F_d$ for any quantity F. In the RH frame the upstream plasma is moving toward the shock surface (assumed to be infinitely thin) with velocity $\mathbf{v}_u$, magnetic field $\mathbf{B}_u$, density ρ_u, and temperature T_u; after the shock, the downstream plasma has velocity $\mathbf{v}_d$, magnetic field $\mathbf{B}_d$, density ρ_d, and temperature T_d (Figure 8). The first four equations above express simple conservation across the shock surface S of mass (Equation (4)), x-momentum (Equation (5)), y-momentum (Equation (6)), and energy flux (Equation (7)), while the last two express, respectively, the consequences of Poisson's equation ($\nabla \cdot \mathbf{B} = 0$) and of Faraday's law ($\nabla \times \mathbf{E} = -\partial \mathbf{B}/\partial t$) across the shock surface. In the above equations, μ is the magnetic

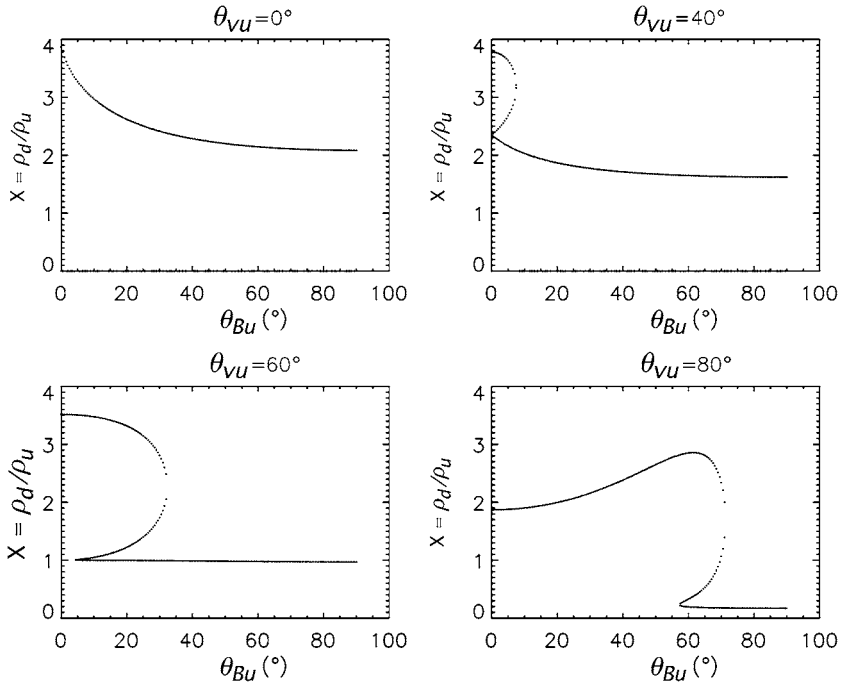

Figure 9. All the possible solutions for the compression ratio $X = \rho_d/\rho_u$ (y-axis) provided by the Rankine–Hugoniot equations as a function of $\theta_{\rm Bu}$ (x-axis) for $\theta_{\rm vu} = 0^\circ$ (top left), $\theta_{\rm vu} = 40^\circ$ (top right), $\theta_{\rm vu} = 60^\circ$ (bottom left), and $\theta_{\rm vu} = 80^\circ$ (bottom right). This figure shows that depending on the values of ($\theta_{\rm Bu}$, $\theta_{\rm vu}$) up to three possible solutions for the compression ratio X are allowed by Rankine–Hugoniot equations.

permeability and γ is the adiabatic index ($\gamma = 5/3$, for a perfect gas).

From the theoretical point of view, given all the upstream plasma parameters ($\mathbf{B}_u$, $\mathbf{v}_u$, ρ_u, T_u), the above equations allow the determination of all the downstream plasma parameters ($\mathbf{B}_d$, $\mathbf{v}_d$, ρ_d, T_d). As previously explained, the upstream plasma density ρ_u and temperature T_u can be both derived from EUV data, while white-light data can be used to estimate the inclination angle $\theta_{\rm Bu}$ of the shock front with respect to the upstream magnetic field B_u, by assuming that, at 4.1 $R_\odot$, $\mathbf{B}_u$ is radial. Moreover, from the shock velocity $v_{\rm sh}$ given above, it is also possible to estimate the upstream velocity vector $\mathbf{v}_u$, i.e., the velocity of the plasma flowing toward the shock surface S in the RH frame. To this end, we assume that, at 4.1 $R_\odot$, also the outflow wind velocity $v_{\rm wind}$ is radial before the shock, thus implying $\mathbf{v}_{\rm wind} \parallel \mathbf{B}$ (see Figure 7). With a value of $v_{\rm wind} \simeq 100$ km s^{-1}, as derived from the intensity ratio $r_{\rm O\,VI} \simeq 2.8$ observed in the pre-shock corona, it turns out that, in the RH frame, $v_{\rm ux} = v_{\rm sh} - v_{\rm wind}\cos\theta_{\rm Bu} \simeq 730$ km s^{-1}, and $v_{\rm uy} = v_{\rm wind}\sin\theta_{\rm Bu} \simeq 72$ km s^{-1}. Hence, $v_u = 734$ km s^{-1} and $\theta_{\rm vu} = \arctan\left(v_{\rm uy}/v_{\rm ux}\right) \simeq 5.^\circ6$, where $\theta_{\rm vu}$ is the angle between the upstream velocity vector and the normal to the shock surface S (see Figure 8). It thus turns out that, from the analysis of the EUV and white-light data, we are able to retrieve all the upstream plasma physical parameters, *except* for the upstream magnetic field strength B_u.

In our case, however, the problem can be solved since, as described above, white-light data also provide us with an estimate of the compression ratio $X = \rho_d/\rho_u$. Hence, the downstream density ρ_d is also known. Unfortunately, given the upstream quantities ($\theta_{\rm Bu}$, v_u, $\theta_{\rm vu}$, ρ_u, T_u) and the downstream density ρ_d, the solution of the above system of equations is not unique. In fact, it can be shown from the above equations that, for the general case of an oblique shock, the quantity X needs to satisfy (Thompson 1962, pp. 86–95) the following cubic equation:

$$0 = \left(M_{\rm Au}^2 - X\right)^2\left\{\gamma\beta_u X + M_{\rm Au}^2\cos^2\theta_{\rm Bu}\left[(\gamma-1)X - (\gamma+1)\right]\right\} + X\,M_{\rm Au}^2\sin^2\theta_{\rm Bu}\left\{\left[\gamma + (2-\gamma)\,X\right]M_{\rm Au}^2 + \left[(\gamma-1)\,X - (\gamma+1)\right]\right\}, \quad (10)$$

where $M_{\rm Au} = v_u/v_{\rm Au}$ and $\beta_u = 2\mu\,p_u/B_u^2$ are, respectively, the upstream Alfvénic number and plasma β parameter. An example of solutions for X provided from the above equation is shown in Figure 9; in particular, this figure shows that for a fixed set (B_u, v_u, ρ_u, T_u) of upstream parameters and a fixed value of the upstream velocity angle $\theta_{\rm vu}$ there are 1, 2, or 3 possible solutions for X, depending on the value of the upstream magnetic field angle $\theta_{\rm Bu}$. These three solutions correspond to a fast, slow, and intermediate shock. More in general, the number of possible solutions for X given from the above equation can be discussed on the ($\theta_{\rm vu}$, $\theta_{\rm Bu}$) plane, as it is shown in Figure 10. The top left panel of this figure shows that there are regions of the ($\theta_{\rm vu}$, $\theta_{\rm Bu}$) plane where the solution for the compression ratio X is unique; this happens for instance where $\theta_{\rm vu} \ll \theta_{\rm Bu}$ and where $\theta_{\rm vu} \gg \theta_{\rm Bu}$. As we concluded above, in our case $\theta_{\rm Bu} = 46.^\circ1$ and $\theta_{\rm vu} = 5.^\circ6$, so that we are in the condition where $\theta_{\rm vu} \ll \theta_{\rm Bu}$, implying that we can limit our analysis to the region of the ($\theta_{\rm vu}$, $\theta_{\rm Bu}$) plane where $\theta_{\rm vu} \ll \theta_{\rm Bu}$. Since in this sub-region of the ($\theta_{\rm vu}$, $\theta_{\rm Bu}$) plane the solution for X is unique, given all the upstream parameters but the unknown magnetic field strength B_u, we are able to determine all the downstream plasma parameters ($\mathbf{B}_d$, $\mathbf{v}_d$, ρ_d, T_d) together with B_u. An example of the solutions in a sub-region of the ($\theta_{\rm vu}$, $\theta_{\rm Bu}$) plane where the solution is unique is shown in panels b–h of Figure 10.

With the above technique, we have derived the following downstream plasma parameters: $T_d = 1.88 \times 10^6$ K ($T_d/T_u = 8.2$), $n_d = 2.26 \times 10^4$ cm^{-3} ($n_d/n_u = 2.06$), $B_d = 0.037$ G ($B_d/B_u = 1.9$), $v_d = 424.4$ km s^{-1} ($v_d/v_u = 0.58$). Hence, as

expected, the downstream plasma is hotter, denser, and slower (in the RH frame) with respect to the upstream plasma; the magnetic field is also compressed, as expected for a fast MHD shock. Given the downstream velocity angle $\theta_{vd} = -33.^{\circ}3$ (in the RH frame), it turns out that, going back to a reference frame at rest with the Sun, the transit of the oblique shock propagating at $v_{sh} = 800$ km s^{-1} increases the post-shock velocity from $v_{pre} \equiv v_{wind} = 100$ km s^{-1} to $v_{post} \simeq 450$ km s^{-1}. This velocity is in good agreement with the value of the ratio $r_{O\,VI}$ as observed in the post-shock corona from UVCS data (Figure 6, right panel). The transit of the shock front also results in a deflection of both the coronal magnetic field and outflow velocity vectors (Figure 11, left panel). In particular, the magnetic field vector is deflected by $\simeq 22.^{\circ}8$ toward the direction parallel to the shock surface (as expected for a fast shock), while the outflow velocity vector (in the reference system at rest with the Sun) is deflected by $\simeq 14.^{\circ}6$ toward the direction perpendicular to the shock surface. Implications from these results are discussed in the next section.

5. DISCUSSION AND CONCLUSIONS

In this work, we analyzed white-light, radio, and EUV data pertaining to a fast CME-driven shock observed in the solar corona on 2002 March 22. This work focuses in particular on the pre- and post-shock corona as observed at 4.1 $R_{\odot}$, where the UVCS slit was positioned during the event. Various signatures of the transit of a shock have been identified in white-light, EUV, and radio data. A first clear signature of the shock transit is provided by radio data a few minutes after the CME initiation, displaying evidence for type II emission associated with an arch-shaped expanding shock front, as detected by the Nançay Radioheliograph at 164.0 MHz, just above the CME source AR. Later on, strong and complex decametric type II emission is also detected. A second clear shock signature is provided by white-light images acquired by the *SOHO*/LASCO coronagraph, showing a arch-shaped region of density increase located above the expanding CME front. Together with the observed deflection of a coronal streamer during the front expansion, this is a clear signature of the plasma compression associated with the transit of the CME-driven shock. A third clear shock signature is provided by EUV spectral data: the transit of the shock across the UVCS slit (located in correspondence of the southward CME flank) results in clear changes in the H I Lyα λ1215.6 and O VI λ1031.9 line intensities, broadenings of the O VI line profiles (representative of post-shock plasma heating) and changes in the O VI λ1031.9/1037.6 line intensity ratio (compatible with post-shock plasma acceleration).

From the observed metric and decametric dynamic spectra, we inferred the existence of a double type II radio burst, whose origin could be attributed to emission from the shock front observed by the Nançay Radioheliograph at 164 MHz and, subsequently, from a flank of the shock surface intersecting a different streamer structure and thus propagating at a much lower speed ($\sim$800 km s^{-1}). The estimated shock speed from this latter component is found to be in outstanding agreement with the one obtained through LASCO and UVCS data in the coronal region studied in this work. Although the timing of the second shock-related type II radio emission was also compatible with the appearance of the other shock signatures observed at 4.1 $R_{\odot}$ in both white-light and EUV data, it was not possible, however, to establish the actual location of this portion of the shock due to the lack of spatial resolution in the observed decametric spectrum.

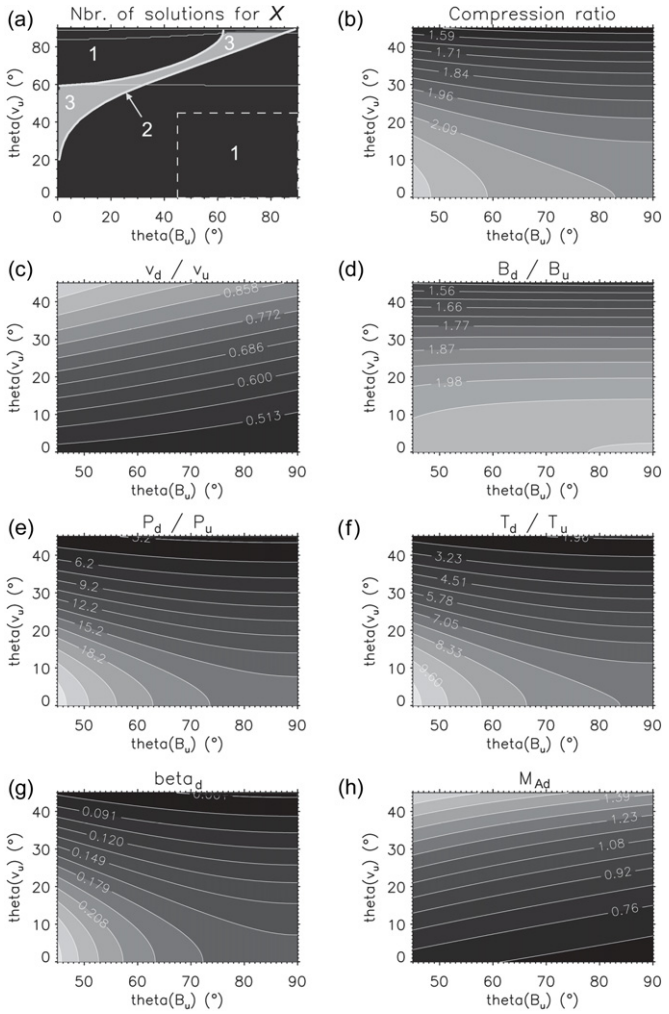

Figure 10. Example of solutions plotted over the plane (θ_{Bu}, θ_{vu}) as provided by the Rankine–Hugoniot equations written for the general case of an oblique shock. Over this plane, these equations have in general 1, 2, or 3 possible solutions for the compression ratio X (panel a). Nevertheless, there are subregions of this plane where a single solution can be determined (white dashed box in panel a). As an example, panels b–h in this figure show the solutions resulting in the sub-region defined by ($45^{\circ} < \theta_{Bu} < 90^{\circ}$, $0^{\circ} < \theta_{vu} < 45^{\circ}$), in particular: the compression ratio X (panel b), the ratio between downstream and upstream velocities (panel c), magnetic fields (panel d), pressures (panel e), temperatures (panel f), and corresponding values of downstream plasma β parameter (panel g) and Alfvénic Mach number M_{Ad} (panel h).

Thanks to the very good time coverage of UVCS data, we have been able to study the physical parameters of the pre-shock corona and their evolution in the post-shock plasma up to $\sim$6 hr after the shock transit. Particularly interesting is the evolution of the O VI $\lambda\lambda$1031.9–1037.6 line profiles observed after the shock transit. Post-shock profiles show significant Doppler shifts, line broadenings, and changes in the 1031.9/1037.6 line intensity ratio, which are indicative, respectively, of motions with component along LOS, plasma heating and bulk expansion, and plasma acceleration. The post-shock O VI $\lambda\lambda$1031.9 line broadening corresponds to an effective kinetic temperature increase of O^{5+} ions by approximately a factor of 2 with respect to the pre-shock corona. Theoretically, this broadening can be due both to the post-shock heating and to the bulk motions associated with the shock and CME expansions. Nevertheless, pre-shock-observed kinetic temperatures are recovered only $\sim$3 hr after the shock transit. This time interval is certainly much longer than the time required for the expanding shock and CME

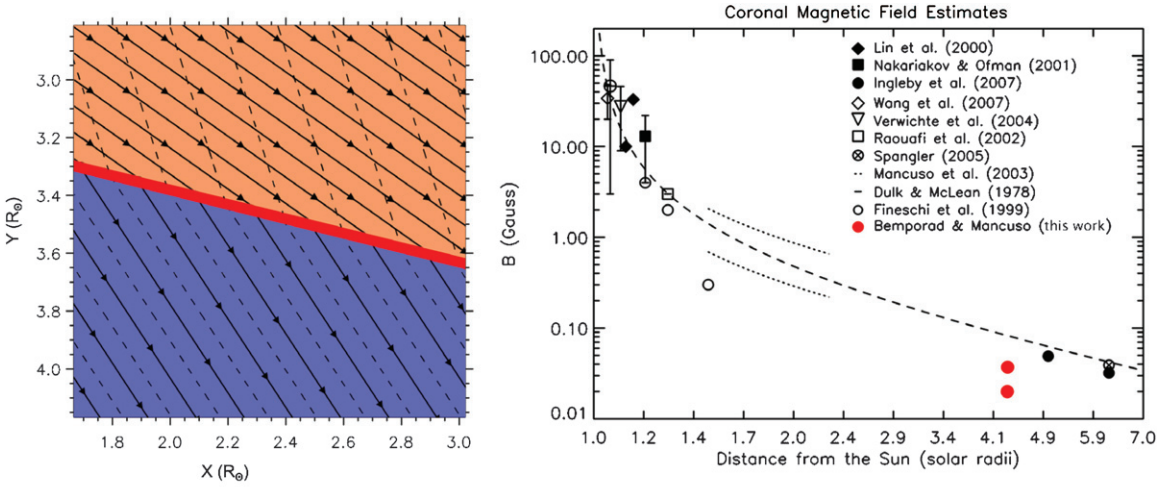

Figure 11. Left: upstream (bottom, light blue) and downstream (top, light red) magnetic field (solid) and stream lines (dashed) in the reference system at rest with the Sun, as we derived from the Rankine–Hugoniot equations. Field and stream lines are plotted in the same coronal region shown in the right panel of Figure 6, for a direct comparison; the upstream and downstream regions are separated by the shock front (red), whose thickness ($\simeq$0.043 $R_\odot$) is plotted to scale. Right: a compilation of coronal magnetic field measurements obtained with different techniques and the estimate of the upstream and downstream magnetic fields (B_u and B_d) involved in the CME-driven shock reported in the present work (red dots).

(A color version of this figure is available in the online journal.)

plasmas (moving at $\sim$800 km s^{-1} where UVCS is observing) to cross the slit's FOV. This suggests that the observed broadening is mainly a thermal effect, because we would expect a much faster decay for the broadening due to the bulk expansion of the shock and CME plasmas. Subsequent evolution shows that $\sim$3 hr after the shock transit the ratio between the intensities of the O VI 1031.9 Å and the O VI 1037.6 Å lines is still much smaller than what observed in the pre-shock corona; this lower ratio indicates that significant plasma outflows are present in the post-shock corona, even $\sim$3 hr after the shock transit. The pre-shock outflows coronal velocities are eventually recovered $\sim$6 hr after the shock transit. Hence, this result indicates that, at the CME flank, the coronal magnetic field left open by the CME transit needs $\sim$6 hr to recover the pre-CME configuration and to slow down the outflowing plasma to the pre-CME coronal values, while at earlier times the angular sector of the corona crossed by the CME has been converted in a faster wind region.

EUV and white-light data have been coupled here to determine all the upstream plasma parameters, but the unknown coronal magnetic field. In particular, from the H I Lyα λ1215.6 and O VI λ1031.9 line intensities observed by UVCS before the shock, we determined the upstream plasma density, temperature, and the pre-shock coronal outflow velocity. At the same time, the white-light intensity observed by LASCO across the shock when the shock was crossing the UVCS slit has been used to estimate the compression ratio at the position of UVCS observations, together with the inclination angle between the shock front and the magnetic and outflow velocity vectors, both assumed to be radial at this altitude. Moreover, from the observed evolution of the H I Lyα line intensity, we derived the shock velocity projected along the UVCS slit which, given the angle between the shock front and the UVCS slit from LASCO image, allowed us to estimate the real shock velocity at the altitude of UVCS observations. The resulting shock velocity is in very good agreement with what we estimated from the analysis of radio data that basically confirm and support, through a set of reasonable assumptions, the above results. Given the above upstream plasma parameters and the compression ratio, we applied the MHD Rankine–Hugoniot equations for the general case of an oblique shock. In general these equations do not provide a unique solution and for this reason they are usually simplified in the two limiting cases of a perpendicular and a parallel shock. Nevertheless, for the event reported here, it is not possible to make one of these simplifying assumptions and we need to apply the general equations. As discussed, there are intervals of possible values of the angles between the upstream velocity and magnetic field vectors and the normal to the shock surface where the general equations give a unique solution; angles for our event fell in one of these intervals. Hence, we have been able to derive from Rankine–Hugoniot equations the full set of post-shock plasma parameters, together with the pre- and post-shock coronal magnetic field. To our knowledge this is the first time that this kind of analysis has been performed in the extended corona to a CME-driven shock.

Our results point to a pre-shock coronal magnetic field at 4.3 $R_\odot$ (the altitude of the UVCS slit westward edge) of $B_u = 0.019$ G, compressed up to $B_d = 0.037$ G after the shock transit. A comparison (Figure 11, right panel) of these values with previous coronal magnetic field estimates derived with many different techniques (e.g., Dulk & McLean 1978; Mancuso & Spangler 2000; Spangler 2005; Ingleby et al. 2007) shows quite good agreement, taking also into account that the well-known Dulk & McLean (1978) magnetic field profile has been derived over an AR, while the magnetic fields reported here refer to a high-latitude coronal region (70° SW). The shock transit leads to electron density and temperature increases by factors 2.06 and 8.2, respectively, starting from the pre-shock coronal values of $n_e = 1.1 \times 10^4$ cm^{-3} and $T_e = 2.3 \times 10^5$ K. This means that across the shock surface the plasma thermal energy density $\epsilon_t = 3\, n\, k_B\, T$ increased by $\Delta\epsilon_t = 1.7 \times 10^{-5}$ erg cm^{-3}, while the magnetic energy density $\epsilon_m = B^2/(2\mu)$ increased by $\Delta\epsilon_m = 4.0 \times 10^{-5}$ erg cm^{-3}. The transit of the shock front also corresponds to a plasma acceleration from the pre-shock outflow speed $v_{\rm pre} \equiv v_{\rm wind} = 100$ km s^{-1} to a post-shock speed $v_{\rm post} \simeq 500$ km s^{-1}, hence to an increase in the kinetic energy density $\epsilon_k = 1/2\, n\, m_p\, v^2$ by $\Delta\epsilon_k = 4.6 \times 10^{-5}$ erg cm^{-3}. As a consequence, the magnetic and kinetic energy density increases are nearly equal (as expected for equipartition of energy), and

are both more than two times larger than the thermal energy increase. In any case, the observed $\Delta\epsilon_t$ is much larger than that expected for a simple adiabatic compression. In fact, in that case we would expect a downstream plasma temperature of

$$T_d = T_u \cdot \left(\frac{n_d}{n_u}\right)^{(\gamma-1)} = T_u \cdot X^{(\gamma-1)}, \quad (11)$$

where X is the compression factor. With $X = 2.06$ (as derived from LASCO data) and $T_u = 2.3 \times 10^5$ K (as derived from EUV data), a simple adiabatic compression would give $T_d = 3.7 \times 10^5$ K, a value much smaller than the $T_d = 1.88 \times 10^6$ K derived from the Rankine–Hugoniot equations.

Pre- and post-shock outflow velocity values are both in good agreement with the observed ratio $r_{\rm O\,VI}$ between the O VI λλ1031.9 and O VI λλ1037.6 lines, which is dependent on the outflow velocity via the Doppler dimming/pumping effect, providing a good validity check to our estimates. The plasma physical parameters given above correspond to local Alfvénic, sound, and magnetosonic velocities of $v_{A,\rm pre} \simeq 400$ km s^{-1}, $v_{s,\rm pre} \simeq 80$ km s^{-1}, and $v_{ms,\rm pre} \simeq 405$ km s^{-1} in the pre-shock coronal plasma; hence the shock, moving at $v_{\rm sh} \simeq 800$ km s^{-1}, is much faster than $v_{\rm ms,pre}$, as expected for a fast shock. After the shock transit, the local Alfvénic, sound, and magnetosonic velocities increase up to $v_{A,\rm post} \simeq 530$ km s^{-1}, $v_{s,\rm post} \simeq 230$ km s^{-1}, and $v_{ms,\rm post} \simeq 580$ km s^{-1}, as a consequence of the density, temperature, and magnetic field post-shock increases. This means that the plasma is outflowing at sub-Alfvénic and supersonic velocities both before and after the shock transit. At the same time, the transit of the shock front corresponds to an increase in the plasma β parameter from $\beta_{\rm pre} \simeq 0.02$ up to $\beta_{\rm post} \simeq 0.1$, due to the relative increase of thermal pressure which is larger (∼16%) than the magnetic pressure increase (∼2.6%).

In conclusion, we showed that, given the white-light, radio, and EUV coronal emissions associated with a CME-driven shock, it is possible to apply the Rankine–Hugoniot equations for the general case of an oblique shock and to derive all the plasma physical parameters in the pre- and post-shock coronal plasmas, including the coronal magnetic field. Even if important information were derived from the analysis of EUV line profiles, we notice that spectroscopic information were not required in our determination of the pre-shock plasma parameters, because only the EUV O VI λ1031.9 and H I Lyα λ1215.6 integrated intensities were employed. Hence, this work demonstrates that coronagraphic observations of CME-driven shocks acquired *at the same time* in white-light and EUV wavelengths can be used to derive the full set of plasma physical parameters involved in coronal shocks.

The authors acknowledge H. Aurass for providing and commenting on the radio data from the Potsdam Observatory, and A. Vourlidas for his comments and advice on the LASCO data. A.B. acknowledges support from ASI/INAF I/023/09/0 contract. *SOHO* is a project of international cooperation between ESA and NASA. The LASCO CME Catalog is generated and maintained by NASA and Catholic University of America in cooperation with the Naval Research Laboratory.

REFERENCES

Bale, S., et al. 1999, Geophys. Res. Lett., 26, 1573
Bemporad, A., et al. 2003, ApJ, 593, 1146
Bemporad, A., Raymond, J. C., Poletto, G., & Romoli, M. 2007, ApJ, 655, 576
Bougeret, J. L., et al. 1995, Space Sci. Rev., 71, 231
Brueckner, R. A., et al. 1995, Sol. Phys., 162, 357
Cairns, I. H. 1986, Proc. Astron. Soc. Aust., 6, 444
Ciaravella, A., Raymond, J. C., & Kahler, S. W. 2006, ApJ, 652, 774
Ciaravella, A., Raymond, J. C., Kahler, S. W., Vourlidas, A., & Li, J. 2005, ApJ, 621, 1121
Cranmer, S. R., et al. 1999, ApJ, 511, 481
Delaboudiniére, J.-P., et al. 1995, Sol. Phys., 162, 291
Doschek, G. A., & Feldman, U. 2004, ApJ, 600, 1061
Dulk, G., & McLean, D. J. 1978, Sol. Phys., 57, 279
Duncan, R. A. 1979, Sol. Phys., 63, 389
Gopalswamy, N. 2006, in AGU Geophysical Monograph Ser. 165, Solar Eruptions and Energetic Particles, ed. N. Gopalswamy, R. Mewaldt, & J. Torsti (Washington, DC: AGU), 207
Gopalswamy, N., et al. 2009, Earth Moon Planets, 104, 295
Gorgutsa, R. V., Gnezdilov, A. A., Markeev, A. K., & Sobolev, D. E. 2001, Astron. Astrophys. Trans., 20, 547
Gosling, J. T., et al. 1974, J. Geophys. Res., 79, 4581
Gouttebroze, P., Lemaire, P., Vial, J. C., & Artzner, G. 1978, ApJ, 225, 655
Ingleby, L. D., Spangler, S. R., & Whiting, C. A. 2007, ApJ, 668, 520
Knock, S. A., Cairns, I. H., Robinson, P. A., & Kuncic, Z. 2001, J. Geophys. Res., 106, 25041
Kohl, J. L., et al. 1995, Sol. Phys., 162, 313
Ko, Y.-K., Li, J., Riley, P., & Raymond, J. C. 2008, ApJ, 683, 1168
Ko, Y.-K., et al. 2003, ApJ, 594, 1068
Lin, H., Penn, M., & Tomczyk, S. 2000, ApJ, 541, L83
Lin, J., Mancuso, S., & Vourlidas, A. 2006, ApJ, 649, 1110
Mancuso, S. 2007, A&A, 463, 1137
Mancuso, S., & Abbo, L. 2004, A&A, 415, L17
Mancuso, S., & Avetta, D. 2008, ApJ, 677, 683
Mancuso, S., & Bemporad, A. 2009, Adv. Space Res., 44, 451
Mancuso, S., & Raymond, J. C. 2004, A&A, 413, 363
Mancuso, S., & Spangler, S. R. 2000, ApJ, 539, 480
Mancuso, S., et al. 2002, A&A, 383, 267
Mancuso, S., et al. 2003, A&A, 400, 347
Mann, G., Aurass, H., Voigt, W., & Paschke, J. 1992, in The First *SOHO* Workshop, Coronal Streamers, Coronal Loops, and Coronal and Solar Wind Composition, ed. C. Mattok (ESA SP-348; Noordwijk: ESA), 129
Mazzotta, P., Mazzitelli, G., Colafrancesco, S., & Vittorio, N. 1998, A&AS, 133, 403
Nelson, G. J., & Melrose, D. B. 1985, in Solar Radiophysics, ed. D. J. McLean & N. R. Labrum (Cambridge: Cambridge Univ. Press), 333
Newkirk, G. 1961, ApJ, 133, 983
Noci, G., Kohl, J. L., & Withbroe, G. L. 1987, ApJ, 315, 706
Ontiveros, V., & Vourlidas, A. 2009, ApJ, 693, 267
Pagano, P., Raymond, J. C., Reale, F., & Orlando, S. 2008, A&A, 481, 835
Raouafi, N.-E., et al. 2004, A&A, 424, 1039
Raymond, J. C., & Ciaravella, A. 2004, ApJ, 606, L159
Raymond, J. C., et al. 2000, Geophys. Res. Lett., 27, 1439
Reiner, M. J., et al. 1997, Geophys. Res. Lett., 24, 919
Reiner, M. J., et al. 2003, ApJ, 590, 533
Saito, K. 1970, Ann. Tokyo Astron. Obs., 12, 53
Sheeley, N. R., Jr., Hakala, W. N., & Wang, Y.-M. 2000, J. Geophys. Res., 105, 5081
Spangler, S. R. 2005, Space Sci. Rev., 121, 189
Thejappa, G., MacDowall, R. J., & Vinas, A. F. 1997, in Proc. 31st ESLAB Symp., Correlated Phenomena at the Sun, in the Heliosphere, and in Geospace, ed. A. Wilson (ESA SP-415; Noordwijk: ESA), 189
The Radioheliograph Group 1993, Adv. Space Res., 13, 411
Thompson, W. B. 1962, An Introduction to Plasma Physics (Reading, MA: Addison-Wesley), 86
Vourlidas, A., Wu, S. T., Wang, A. H., Subramanian, P., & Howard, R. A. 2003, ApJ, 598, 1392
Wild, J. P. 1950, Aust. J. Sci. Res., A3, 541